



A Comparison of Optimal, Binary Closed-Loop Active Flow Control Applied to an Annular Compressor Stator Cascade with Periodic Disturbances

Benjamin Fietzke¹(✉), Jan Mihalyovics², Rudibert King¹, and Dieter Peitsch²

¹ Department of Process Engineering, Chair of Measurement and Control, Technische Universität Berlin, 10623 Berlin, Germany

B.Fietzke@tu-berlin.de

² Institute of Aeronautics and Astronautics, Chair for Aero Engines, Technische Universität Berlin, 10587 Berlin, Germany

Jan.Mihalyovics@tu-berlin.de

Abstract. Pressure gain combustion has been proposed to exploit superior thermodynamic cycles in gas turbines. However, further research on their integration is needed to reduce the induced negative effects on the last stages of a compressor. In this contribution, mitigation results on the effects of periodic disturbances on an annular compressor stator rig are presented and compared for different closed-loop controllers. Instead of a real, unsteady combustion setup, a rotating disc was installed to create periodic disturbances downstream of each passage. Pneumatic active flow control served to influence the suction side of each stator blade.

With steady blowing actuation, the effects of periodically induced disturbances could not be explicitly addressed and led to worse results compared to the closed-loop versions. For closed-loop control, a clear recommendation for a class of learning approaches can be given. Finally, an evaluation of the efficiency of flow control is presented with a refined characterization of the actuation effort.

Keywords: Closed-loop control · Active flow control · MPC · ILC · RMPC · Annular compressor stator cascade · Pulsed jets

1 Introduction

The performance of modern gas turbine compressors is limited by flow separation from the suction side of the stator and rotor blades. Therefore, in general, a compressor blade is designed to avoid boundary layer separation, limiting the amount of achievable flow turning and pressure rise from a single blade row and hence an axial compressor stage. However, the loading of such blades and the risk of separation increases significantly when pressure gain combustion (PGC) is integrated due to its unsteady effects on the upstream flow field. To mitigate these effects and still benefit from PGC, the application of active flow control (AFC) is proposed.

Previous studies have shown that actively controlling the secondary flow features within a passage can lead to higher pressure recoveries of a stator vane [1]. A comprehensive review of a wide variety of possible actuator concepts is presented by Cattafesta et al. [2]. Of those concepts, pneumatic actuation by air injection is particularly interesting for axial compressors, as bleed air can be used.

However, recent studies [11] of a linear stator cascade have shown an overall efficiency drop with increasing actuation amplitudes for blowing. Therefore, the actuation effort should be as low as possible while damping the induced disturbances of PGC.

In this paper, the results of an annular compressor stator cascade with AFC are discussed. An annular test rig was equipped with highly loaded stator vanes and an end-wall actuator at the hub side of each passage. In the experiments, air blowing out of rectangular actuation slots was modulated using solenoid valves, thus requiring a binary control signal. In addition to steady blowing, different closed-loop concepts were applied and compared—two variants of model predictive controllers (MPCs), a quadratic iterative learning controller (QILC), and a repetitive model predictive controller (RMPC). Both the QILC and RMPC exploit the periodic character of the induced disturbances and have already been successfully adapted with a real-valued control signal and proportional valves in a linear stator cascade [10]. For the MPCs, a simple disturbance model and an extended disturbance model are proposed here to estimate and predict the disturbance.

Within all four closed-loop algorithms, an optimal binary control signal had to be calculated with respect to a chosen cost function. This led to a binary quadratic program (BQP) and was solved with a classical branch-and-bound (B&B) [6] algorithm combined with an underlying quadratic program solver [5] to obtain the optimal solution of the BQP in real time.

2 Experimental Setup

In this section, the setup for the annular stator cascade experiments is briefly explained. All experimental investigations were conducted using a low-speed, open circuit wind tunnel at the Chair for Aero Engines. The annular design was chosen to create enhanced three-dimensional flow characteristics and thus enable investigation of the effects of unsteady disturbances at a high spatial resolution.

The annular setup consisted of a highly loaded compressor stator cascade equipped with controlled diffusion airfoils. A schematic of the cascade and the airfoil geometry is presented in Fig. 1a. The blades were designed to produce an axial outflow with a chord-based Reynolds number of $Re = 6 \times 10^5$ without any gap at the hub or tip and with a total mass flow of $\dot{m}(k) \approx 9.3 \text{ kg/s}$ at every time step k . Downstream of the cascade, a rotating throttling disc was installed (Fig. 1b) to mimic periodic disturbances that could occur using downstream PGC. During the experiments, the disc ran at a frequency of 3.7 Hz, which led to a disturbance frequency of $f_d = 7.4 \text{ Hz}$ and a resulting Strouhal number of

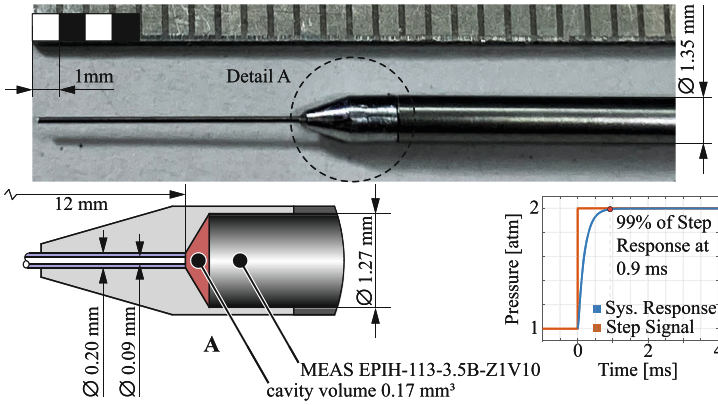


Fig. 2. Miniature pitot tube probe

A jet actuator system with binary controlled solenoid valves (Fig. 1a; bottom) was used to influence the flow via pneumatic blowing. The actuation system was located on the hub wall side and consisted of a rectangular outlet orifice, with slot height $h_{act}/c = 0.053$ and slot width $d_{act}/c = 0.001$ in relation to the blade chord length c (Fig. 1a). The outlet orifices had a blowing angle of $\Theta = 15^\circ$ relative to the passage end wall and were oriented perpendicular to the blade’s surface. Further information on the jet actuator system can be found in [4].

To assess the outflow conditions of the additively manufactured actuators, a miniature pitot tube (MPT) was used during additional actuator slot experiments. The MPT featured a sub-miniature pressure sensor [MEAS EPIH-113-3.5B-Z1V10] with an outer diameter of only 1.27 mm specifically designed for dynamic and high-frequency measurements. The MPT’s slender inlet tube had an outer diameter of 0.2 mm, an inner diameter of 0.09 mm, and a length of 12.00 mm. Thus, the MPT had a blockage of less than 1% with respect to actuator slot height of 0.4 mm and length of 10.00 mm. The pressure sensor did not have a screen or any protective coatings on the diaphragm, and the cavity volume in the MPT was kept to a minimum of only 0.17 mm^3 (see Fig. 2). Using the analysis of line-cavity systems presented in [3] to model the linearized dynamic of a pneumatic measuring system, one can state that the geometric parameters of the MPT yield a bandwidth of approximate 1070 Hz, thus being sufficiently fast for the presented measurements. The MPT was traversed in a cartesian grid covering 30 points in the exit plane of the actuator slot. The grid had three points in d - and ten points in the h -direction.

The amplitude of actuation is represented here by the momentum coefficient $c_\mu(k)$. It describes the momentum of an actuated passage with actuation mass flow $\dot{m}_{jet}(k)$ and properly defined velocity $v_{jet}(k)$; (see below) in relation to the momentum of a passage flow in the cascade:

$$c_\mu(k) = \frac{\dot{m}_{jet}(k) \cdot v_{jet}(k)}{A_{psg} \cdot q_{1,ref}(k)} = \frac{\dot{m}_{jet}^2(k)}{A_{psg} \cdot q_{1,ref}(k) \cdot \rho \cdot d_{act} \cdot h_{act}}. \quad (1)$$

with:

$$\dot{m}_{jet}(k) = \begin{cases} \frac{\dot{m}_{act}(k)}{n_{act}(k)} & n_{act}(k) > 0 \\ 0 & n_{act}(k) = 0 \end{cases}. \quad (2)$$

Hereby, $n_{act}(k)$ represents the number of actuated passages, A_{psg} the cross sectional area of one passage, $q_{1,ref}$ the dynamic pressure measured upstream of the passage on the reference location, and ρ represents the density of air. During the closed-loop and open-loop wake measurements, it was not possible to measure v_{jet} and verify whether it was homogenous over the actuator slot. Therefore, a mean v_{jet} was estimated via linear interpolation, using the results of the actuation slot measurements obtained from a separate experiment (see Fig. 5). Finally, the resulting values of c_μ could be calculated.

3 Closed-Loop Control

In [4], without the refined actuation slot measurements, we already compared open-loop actuation against RMPC. Additionally, more details with respect to RMPC and the chosen surrogate control variable for the test rig were given. In the following, we repeat only some of the details and introduce other controllers used in the comparison.

3.1 Model Identification

With a surrogate control variable, a scalar was introduced that best reflected the results of the flow disturbances. For time step k , it describes the disturbance impact on the static pressure coefficients of the control blade and reads as

$$y_k = \underline{p}_1^T \cdot \underline{c}_p(k) - y_s \quad . \quad (3)$$

Here, \underline{p}_1^T is the first principle component of the control blade's disturbed static pressure coefficients. The vector $\underline{c}_p(k)$ comprises measurements from ten sensor locations (see Sect. 2.1), and y_s describes a constant operating point. As a consequence, when $y_k = 0$, the variance of the disturbance's impact along the direction given by \underline{p}_1 is zero, which is the overall goal of the closed-loop control. Therefore, the reference for closed-loop control is set to $r_k = 0$.

In Eq. (3), \underline{p}_1 can be understood as a weighting vector for the influence of the control blade's static pressure sensors on y_k . Figure 3a presents a plot of \underline{p}_1 over the sensor positions of the control blade. Because \underline{p}_1 decreases over the suction side coordinate s , the last sensors have a significantly less effect on y_k than the first ones. In Fig. 3b, y_k is shown over the cycle of one disturbance period.

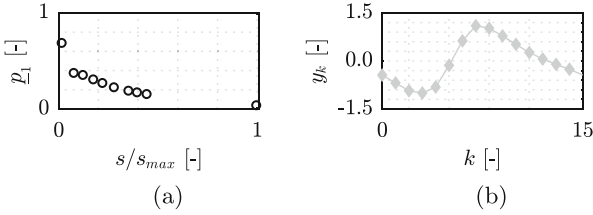


Fig. 3. First principle component of disturbance influence on $c_p(k)$ (a) and its time-dependent projection on p_1 (b).

For modeling, a system excitation was performed for different actuation amplitudes and blowing distributions with respect to the actuated passages. Pseudorandom binary signals were used as valve control signals to identify a linear, time-invariant, discrete-time single-input single-output state-space model for the actuation valves’ physically possible frequency range.

All control algorithms applied in this study will be based on a prediction of the future evolution of the systems’ state and control error. With the identified model, these predictions will only depend on the actual state at time k and the future undetermined evolution of the control input. The predictions can be given in a very compact form introducing appropriately built matrices \mathbf{F} and \mathbf{G} to describe the influence of the actual state and predicted control input on the future evolution of the control error; see [4]. In all control algorithms, an optimization problem will be solved based on optimization criteria I evaluating the outcomes of the predictions.

3.2 Controller Formulation

In the following, the formulation of all used control algorithms is shown. We start with the RMPC formulation, the derivation of which is shown in more detail in [4]. With relatively minor adjustments, the formulations of the MPC and the QILC can finally be derived by modifying the optimization criteria.

RMPC. In an RMPC, the prediction of the system’s output error $e_k = r_k - y_k$ makes use of the knowledge of the periodic disturbance \mathbf{d}_{k-n} of the last cycle and assumes that this disturbance will occur again. The matrix \mathbf{G} maps the supposed control input trajectory $\mathbf{u}_{k|k}$ and \mathbf{F} maps the initial state error $\mathbf{\varepsilon}_k$ to the predicted error trajectory $\mathbf{e}_{k+1|k}$. In the following, a vector with the notation $(\cdot)_{k|k}$ and $(\cdot)_{k+1|k}$ indicates a prediction at current time step k for future values starting at k and $k+1$, respectively. With the special notation $(\cdot)_{k+n|k}$, the last entry of a prediction vector is addressed. $(\cdot)_{k-n}$ refers to the corresponding trajectory of the last cycle, $\Delta(\cdot)$ refers to the change in comparison to the last cycle, and (\cdot) refers to the last row of the corresponding matrix.

The cost function $I(\mathbf{u}_{k|k})$ of the optimization problem, depending on $\mathbf{u}_{k|k}$, is defined by the summation of the prediction’s running costs and end costs. As

our identified system is asymptotically stable, we can ensure stability for the closed-loop system with an adequate set of weight matrices. These are for the future error \mathbf{W}_e , future control input \mathbf{W}_u , change in control input with respect to the last cycle \mathbf{W}_Δ , and the end costs \mathbf{W}_e . $I(\mathbf{u}_{k|k})$ can finally be written as a quadratic function² with the Hessian matrix \mathbf{H} and a linear term \underline{f}_k^T . Thus, the binary optimization problem to calculate the optimal control trajectory $\mathbf{u}_{k|k}^*$ is

$$\mathbf{u}_{k|k}^* = \underset{\mathbf{u}_{k|k}}{\operatorname{argmin}} \left\{ \overbrace{\mathbf{u}_{k|k}^T \mathbf{H} \mathbf{u}_{k|k} + \underline{f}_k^T \mathbf{u}_{k|k}}^{I(\mathbf{u}_{k|k})} \right\} , \quad (4a)$$

subject to

$$\mathbf{u}_{k|k} \in \mathbb{B}^n , \quad (4b)$$

with

$$\mathbf{H} = \mathbf{G}^T \mathbf{W}_e^T \mathbf{G} + \mathbf{W}_u + \mathbf{W}_\Delta + \frac{1}{2} \check{\mathbf{G}}^T \mathbf{W}_e \check{\mathbf{G}} , \quad (5a)$$

$$\underline{f}_k^T = -2 \left(\underline{\mathbf{s}}_{k+1|k}^T \mathbf{W}_e \mathbf{G} + \underline{\mathbf{u}}_{k-n}^T \mathbf{W}_\Delta + \frac{1}{2} t_{k+n|k}^T \mathbf{W}_e \check{\mathbf{G}} \right) , \quad (5b)$$

$$\underline{\mathbf{s}}_{k+1|k} = \underline{\mathbf{e}}_{k-n} + \mathbf{F} \Delta \underline{\varepsilon}_k + \mathbf{G} \underline{\mathbf{u}}_{k-n} , \quad t_{k+n|k} = e_k + \check{\mathbf{F}} \Delta \underline{\varepsilon}_k + \check{\mathbf{G}} \underline{\mathbf{u}}_{k-n} . \quad (5c)$$

As solenoid valves were used for actuation, the design variables of this and the following optimization problem are binary (Eq. (4b)). The first input of the optimal control trajectory $\mathbf{u}_{k|k}^*(1)$ is used as control input u_k for the control blade's passage valve, while at the next time step $k+1$ the optimization problem has to be solved again. This "principle of receding horizon" is part of every model predictive control used in this study.

MPC. In contrast to the RMPC, the past cycle is not taken into account in an MPC, so that the cyclic character of the disturbance induced by the throttling disc is not exploited. Instead, a prediction of the disturbance is used, see below. Moreover, all terms relating to the last cycle are dropped. Thus, the structure of the BQP is the same (Eq. (4)), but with slightly different matrices

$$\mathbf{H} = \mathbf{G}^T \mathbf{W}_e^T \mathbf{G} + \mathbf{W}_u + \frac{1}{2} \check{\mathbf{G}}^T \mathbf{W}_e \check{\mathbf{G}} , \quad (6a)$$

$$\underline{f}_k^T = -2 \left(\underline{\mathbf{s}}_{k+1|k}^T \mathbf{W}_e \mathbf{G} + \frac{1}{2} t_{k+n|k}^T \mathbf{W}_e \check{\mathbf{G}} \right) , \quad (6b)$$

$$\underline{\mathbf{s}}_{k+1|k} = \mathbf{F} \underline{\varepsilon}_k - \underline{\mathbf{d}}_{k+1|k} , \quad t_{k+n|k} = \check{\mathbf{F}} \underline{\varepsilon}_k - d_{k+n|k} . \quad (6c)$$

QILC. In contrast to the two other controllers, QILC is not based on the receding horizon principle, but the control trajectory of the upcoming cycle is

² The offset of the cost function is ignored here because it is not essential for the optimization program.

calculated from the control trajectory and the remaining control error of the last cycle by an optimization program [10].

$$I(\underline{\mathbf{u}}_j) = \underline{\mathbf{u}}_j^T \mathbf{H} \underline{\mathbf{u}}_j + \underline{f}_j^T \underline{\mathbf{u}}_j \quad (7a)$$

with

$$\mathbf{H} = \mathbf{G}^T \mathbf{W}_e \mathbf{G} + \mathbf{W}_u + \mathbf{W}_\Delta \quad , \quad (8a)$$

$$\underline{f}_j^T = -2 (\underline{\mathbf{s}}_j^T \mathbf{W}_e \mathbf{G} + \underline{\mathbf{u}}_{j-1}^T \mathbf{W}_\Delta) \quad , \quad (8b)$$

$$\underline{\mathbf{s}}_j = \underline{\mathbf{e}}_{j-1} + \mathbf{F} \Delta \varepsilon_{0,j} + \mathbf{G} \underline{\mathbf{u}}_{j-1} \quad . \quad (8c)$$

This BQP is solved only once at the start of each cycle, and the entire control trajectory is applied. In the case of QILC, the notation $(\cdot)_j$ indicates a trajectory for the current cycle and $(\cdot)_{j-1}$ indicates a trajectory for the last cycle. Additionally, within the QILC formulation there is no term regarding the end costs because when using a QILC it is usually assumed that the initial conditions are always constant, which was approximately the case during the experiments.

Finally, the setup for the learning weight \mathbf{W}_Δ for the RMPC and QILC, with equal diagonal entries of $w_\Delta \in \mathbb{R}_{>0}$ will be discussed here. As suggested in [7], w_Δ is implemented as an adaptive parameter to account for peculiarities of the binary domain. In contrast to the case of real-valued control signals, for a fixed $w_\Delta \gg 0$, the binary solution for $\underline{\mathbf{u}}_{k|k}^*$ is likely to get stuck in a sub-optimal solution. Therefore, it is checked whether the control signal trajectory has changed at every time step compared to the previous cycle. If this is not the case, w_Δ is reduced by 5%, to allow for a possible higher change for the next optimal control trajectory.

Since in case of the QILC the corresponding BQP only has to be solved once per cycle, in every remaining time step³ w_Δ can be adapted to solve the BQP of the last cycle start, with lowered w_Δ until a change in the optimal control signal trajectory occurs. The changed w_Δ then influences the trajectory in the next cycle. The weight adaptation is done until w_Δ falls below a small threshold of 0.01, where both the RMPC and QILC are likely to be converged. After that, w_Δ is set back to the initial value of $w_{\Delta,0} = 100$.

3.3 State Estimation

Since the state vector is not directly measurable, a Kalman filter is used to calculate the estimated state $\hat{\mathbf{x}}_k$ and, by this, the estimated state error $\hat{\mathbf{e}}_k$ needed for the MPC and RMPC. To improve the quality of the estimation, we introduce disturbance models. In the case of the MPC, a disturbance model is even mandatory to estimate the disturbance d_k and predict the future disturbance trajectory $\underline{\mathbf{d}}_{k+1|k}$, Eq. (6).

Two approaches for the disturbance model were investigated. The first one assumes the disturbance as a constant offset δ_k . Therefore, within the MPC, the

³ Meaning the $n - 1$ time steps that are not used for solving the original BQP.

vector $\underline{\mathbf{d}}_{k+1|k}$ is held constant at δ_k during a prediction horizon. With \mathbf{A} being the matrix of the identified state-space model, $\underline{\mathbf{b}}$ and $\underline{\mathbf{c}}$ being the input and output vectors, and $\underline{\mathbf{x}}_k$ being the corresponding state-space vector, the augmented state-space model, including the constant disturbance model, reads

$$\begin{pmatrix} \underline{\mathbf{x}}_{k+1} \\ \delta_{k+1} \end{pmatrix} = \begin{bmatrix} \mathbf{A} & \mathbf{O} \\ \mathbf{O} & 1 \end{bmatrix} \begin{pmatrix} \underline{\mathbf{x}}_k \\ \delta_k \end{pmatrix} + \begin{bmatrix} \underline{\mathbf{b}} \\ 0 \end{bmatrix} u_k \quad , \quad (9a)$$

$$y_k = [\underline{\mathbf{c}}^T \ 1] \begin{pmatrix} \underline{\mathbf{x}}_k \\ \delta_k \end{pmatrix} \quad , \quad (9b)$$

with \mathbf{O} as the zero matrix/vector of the corresponding dimension.

Inspired by the similarity of the induced disturbances with a harmonic oscillation (compare Fig. 3b), an oscillating second-order system with zero damping and a state vector $\underline{\mathbf{z}}_k \in \mathbb{R}^2$ is included in Eq. (9) to define a second dynamic disturbance model within the augmented state-space model:

$$\begin{pmatrix} \underline{\mathbf{x}}_{k+1} \\ \underline{\mathbf{z}}_{k+1} \\ \delta_{k+1} \end{pmatrix} = \begin{bmatrix} \mathbf{A} & \mathbf{O} & \mathbf{O} \\ \mathbf{O} & \mathbf{A} & \mathbf{O} \\ \mathbf{O} & \mathbf{O} & 1 \end{bmatrix} \begin{pmatrix} \underline{\mathbf{x}}_k \\ \underline{\mathbf{z}}_k \\ \delta_k \end{pmatrix} + \begin{bmatrix} \underline{\mathbf{b}} \\ 0 \\ 0 \\ 0 \end{bmatrix} u_k \quad , \quad (10a)$$

$$y_k = [\underline{\mathbf{c}}^T \ 1 \ 0 \ 1] \begin{pmatrix} \underline{\mathbf{x}}_k \\ \underline{\mathbf{z}}_k \\ \delta_k \end{pmatrix} \quad . \quad (10b)$$

Here, \mathbf{A} is chosen so that the eigenfrequency of the second-order system is equal to f_d . Within the MPC, the matrix \mathbf{A} and the estimated disturbance state vector $\underline{\mathbf{z}}_k$ can be used to calculate a dynamic prediction $\underline{\mathbf{d}}_{k+1|k}$, which is more accurate than the first approach above.

Finally, each augmented state-space model is used in a corresponding Kalman filter to calculate the augmented state vector. The equations and settings for a Kalman filter are well documented in the literature (e.g., see [8]).

4 Results

The outcome of the actuation slot measurements are presented first, followed by the results of the closed-loop experiments. Finally, a series of open-loop wake measurements are presented, comparing the impact of steady blowing and the RMPC control trajectory on important characteristics of the considered passage.

4.1 Actuation Slot Experiments

Figure 4 shows an example of the time-averaged velocity field measured at the actuator slot outlet using the MPT for the lowest ($p_{act} = 2$ bar) and the highest set pressure in the actuator pressure tank ($p_{act} = 4$ bar). It can be seen that the velocity field is relatively uniformly distributed, especially at a higher pressure.

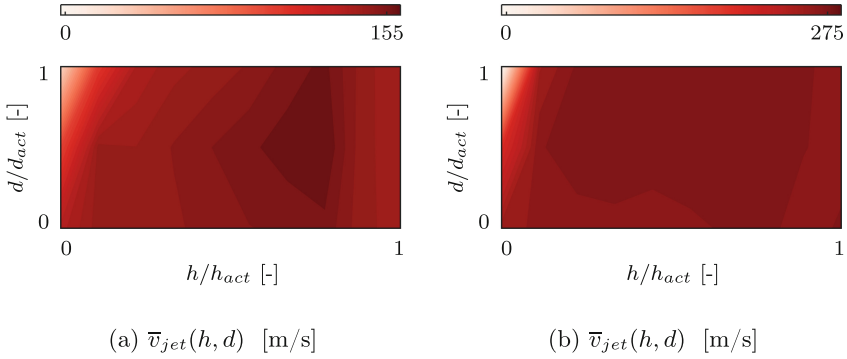


Fig. 4. Time-averaged velocity field in the actuator slot for (a) $p_{act} = 2$ bar and (b) $p_{act} = 4$ bar.

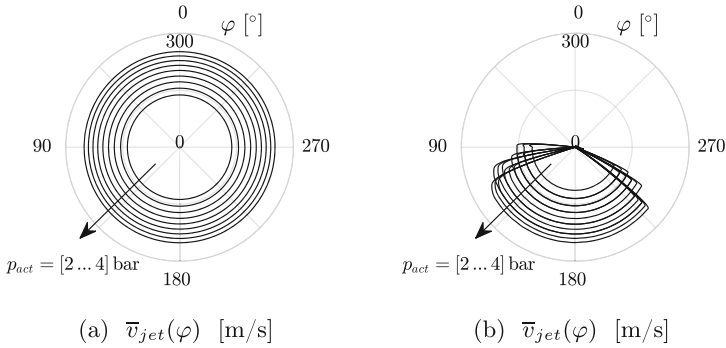


Fig. 5. Area-averaged actuator slot velocity over a mean period φ over $p_{act} = [2...4]$ bar for (a) steady actuation and (b) applied RMPC trajectories.

The velocity drops to nearly zero only at a measurement point in the upper left corner, as this actuator slot was blocked due to manufacturing tolerances decreasing the effective outlet area.

The area-averaged jet velocity for a mean period⁴ $\varphi = [0...360]^\circ$ for a range of different p_{act} is displayed in Fig. 5. Figure 5a shows the results for steady blowing, and Fig. 5b shows the results for several RMPC trajectories and pressure levels. The outlet velocities can be estimated using linear interpolation, and the corresponding c_{μ} values can be calculated retrospectively for the open-loop measurements previously presented in [4].

⁴ Note: Because the disturbance induced by the throttling disc is periodic, a period angle φ can be defined.

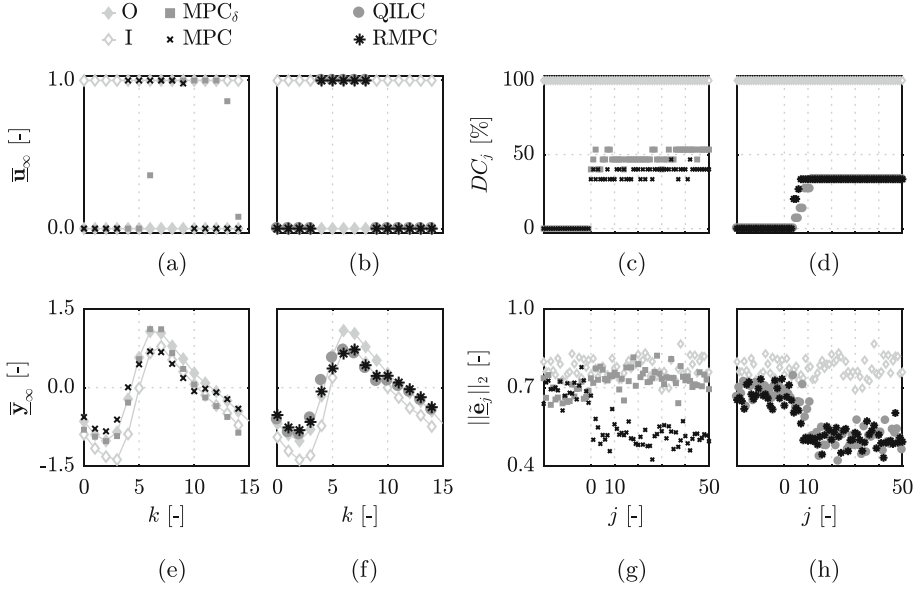


Fig. 6. Comparison of different closed-loop actuations. On the left, the two MPCs (a, e) and learning controllers (b, f) are shown and compared with the non-actuated case (O) and the permanently actuated case (I) over an averaged cycle. On the right, the duty cycle and normalized control error norm are shown over several cycles for the two MPCs (c, g) and the learning controllers (d, h).

4.2 Closed-Loop Experiments

Figure 6 shows the results of the closed-loop experiments with different controller configurations compared with the base case (O - *grey diamonds*) and the case with steady actuation (I - *grey diamonds*). The *squares* show the data for the MPC with the Kalman filter using the simple disturbance model (Eq. (9)). The *crosses*, *circles*, and *stars* show the data for MPC, QILC, RMPC with the Kalman filter using the extended disturbance model (Eq. (10)). On the left side, the averaged, converged control trajectories $\bar{\mathbf{u}}_\infty$ and output trajectories $\bar{\mathbf{y}}_\infty$ over the time steps k of a disturbance cycle j are presented. The notation $(\cdot)_\infty$ indicates that the considered number of cycles before averaging was high enough so that the learning controllers could converge. In terms of the two MPCs, the control trajectories were still slightly fluctuating because, in contrast to the learning controllers, the change of control trajectory is not penalized. This can be observed from the non-binary⁵ values of $\bar{\mathbf{u}}_\infty$ of the MPCs (Fig. 6a), which is not the case for QILC and RMPC that reached a converged state (Fig. 6b).

As discussed above, $\bar{\mathbf{y}}_\infty = \mathbf{0}$ means that the influence of the throttling disc on the first principle component of the pressure readings on the suction side disappears. Without control (O), $\bar{\mathbf{y}}_\infty$ clearly deviates from zero, which indicates

⁵ This results when fluctuating binary trajectories are averaged over several cycles.

the disturbance's influence (Figs. 6e and 6f). For open-loop control with steady actuation (I), the absolute value of \bar{y}_∞ could only be decreased for very few time instants, while in other phases, the results were even worse. Looking at the results of the MPC with the simple disturbance model (MPC $_\delta$), the same holds here as well: the disturbance could not be effectively damped. However, the MPC with the enhanced disturbance model was able to lower the disturbance impact much more, similar to the effect of the QILC and RMPC (Fig. 6f).

On the right side of Fig. 6, the convergence behavior of the controllers with respect to the duty cycle DC_j of the actuation and the relative 2-norm of the output error trajectory \underline{e}_j of a period j

$$\|\underline{\hat{e}}_j\|_2 = \|\underline{e}_j\|_2 / \sqrt{n} \quad (11)$$

can be seen. All controllers were activated at $j = 0$. The RMPC and the QILC converged after seven and twelve cycles, respectively, and lowered the error from $\|\underline{\hat{e}}_j\|_2 \approx 0.68$ to $\|\underline{\hat{e}}_j\|_2 \approx 0.50$ (Fig. 6h), an improvement of about 25%. The duty cycle of the valves was constant at $DC_j = 33\%$ after convergence (Fig. 6d). With steady actuation and the MPC with the simple disturbance model, the error even increased (Fig. 6g), while DC_j , and thus the actuation effort, was higher (Fig. 6c). The MPC with enhanced disturbance model lowered the error similar to the learning controllers but was faster due to the missing costs of control trajectory change. In return, DC_j was on a slightly higher level and fluctuated more.

The closed-loop experiment with the RMPC, presented in Fig. 6, was conducted five times for every considered actuation amplitude. The converged RMPC trajectories were then averaged and used for the following wake measurements.

Open-Loop Wake Experiments

In this section, the effect of the RMPC trajectory on the wake of a passage and particularly three important characteristics of the passage will be shown. The c_μ -values were calculated with the data of Fig. 5 and are more accurate than the c_μ -values in our previous publication [4].

Keeping in mind the overall purpose of a stator vane—the conversion of dynamic pressure into static pressure—the static pressure rise coefficient $C_p(z, y, k)$ of a passage is an important parameter. It is defined as the difference between the local static pressure downstream $p_2(z, y, k)$ and the area-averaged static pressure upstream $\bar{p}_1(k)$ of the passage relative to the mass-averaged upstream dynamic pressure $\bar{q}_1(k)$

$$C_p(z, y, k) = \frac{p_2(z, y, k) - \bar{p}_1(k)}{\bar{q}_1(k)}. \quad (12)$$

Note that as suggested by Cumpsty and Horlock [9], area-averaging is used for static pressure and mass averaging is used for total and dynamic pressure.

In comparison to $C_p(z, y, k)$, the total pressure loss coefficient $\zeta^*(z, y, k)$ takes the difference of the total pressure into account

$$\zeta^*(z, y, k) = \frac{\bar{g}_1^*(k) - g_2(z, y, k)}{\bar{q}_1(k)}, \quad (13)$$

with the corrected inlet total pressure of the passage

$$\bar{g}_1^*(k) = \frac{\dot{m}_{psg}(k) \cdot \bar{g}_1(k) + \dot{m}_{act,psg}(k) \cdot p_{act}(k)}{\dot{m}_{psg}(k) + \dot{m}_{act,psg}(k)}, \quad (14)$$

including the contribution of the actuation mass flow as well. Here, $\dot{m}_{act,psg}(k)$ is the measured passage's actuation mass flow and $p_{act}(k)$ is the total pressure of the actuation, defined as the pressure in the actuation stagnation tank.

Since our definition of the actuation amplitude $c_\mu(k)$ (Eq. (1)) does not allow for an evaluation of the overall mass flow effort of a specific passage for pulsed actuation, the last characteristic describes the actuation mass flow of a specific passage $\dot{m}_{act,psg}(k)$ in relation to the passage's inlet mass flow $\dot{m}_{psg}(k) = \dot{m}(k)/n_s$

$$\mu(k) = \frac{\dot{m}_{act,psg}(k)}{\dot{m}_{psg}(k)} \quad . \quad (15)$$

Here, $\dot{m}_{act,psg}(k)$ is approximated with the general jet mass flow $\dot{m}_{jet}(k)$ weighted with the control input $u_{k,psg}$ for the valve of the specific passage

$$\dot{m}_{act,psg}(k) = \dot{m}_{jet}(k) \cdot u_{k,psg} \quad . \quad (16)$$

To compare the effects of different actuation amplitudes c_μ on the passage characteristics, $C_p(z, y, k)$ was area-averaged and $\zeta^*(z, y, k)$ was mass-averaged. Both characteristics were also phase-averaged and divided by the corresponding characteristic value for the case without actuation. Whereas $\mu(k)$ was phase-averaged. The outcome is shown in Fig. 7 over different c_μ values. It can be seen that with increasing c_μ , the positive effect on the static pressure rise of

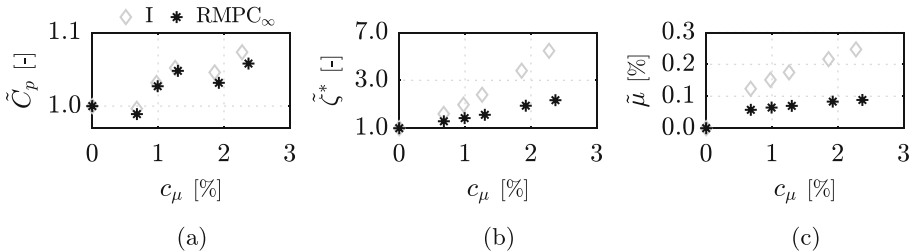


Fig. 7. Normalized mean static pressure rise coefficient (a), corrected total pressure loss coefficient (b), and actuation mass flow consumption (c) for base flow ($c_\mu = 0\%$), steady blowing, and RMPC actuation for different actuation amplitudes.

RMPC-enabled actuation was just moderately lower compared to steady actuation. However, for the latter, the consumption of actuation mass flow was up to three times higher, while the total pressure loss coefficient was up to two times higher than with RMPC actuation. Consequently, using RMPC-enabled AFC, the efficiency drop was significantly lower while producing a comparable rise in static pressure.

5 Conclusion

An annular low-speed compressor stator rig with hub-sided pneumatic AFC was investigated. Downstream of the stator vanes, a rotating throttling disc was installed to mimic the effect of periodic disturbances as they could occur with the usage and integration of pressure gain combustion concepts. Previous investigations of a linear compressor stator rig [11] indicated that although the flow field in a stator row can be manipulated effectively, the overall efficiency of the cascade will decrease with higher actuation amplitudes. Therefore, different advanced closed-loop concepts were applied to test their performance in reducing the impact of the periodic disturbances and decreasing the effort of actuation mass flow compared to steady actuation. To that end, a scalar surrogate control variable was specified for a control blade equipped with high-bandwidth pressure sensors, and an input-output model was identified to predict the influence of the binary actuation on the defined control variable. In addition, two different disturbance models were included in the control algorithms for state estimation and disturbance prediction.

It could be shown that an MPC with the simple disturbance model could not lessen the disturbance impact. In contrast, an MPC with the extended disturbance model could damp the disturbances effectively. The two applied learning controllers, a QILC and an RMPC, performed even better due to the ability to learn from past disturbance cycles. In our case, this resulted in a smooth, converging control trajectory and slightly less actuation effort. Comparing the QILC and the RMPC, the latter converged slightly faster, which is based on the receding horizon principle applied within the RMPC algorithm. With the exception of the MPC with the simple disturbance model, all closed-loop approaches lowered the relative 2-norm of the disturbance impact on the control variable up to 25%. For this control task, the performance with steady actuation was insufficient and not suited to lessening the disturbance's effects. With several RMPC runs, an optimal input trajectory for each actuation amplitude c_μ was obtained and thereafter used for further open-loop wake experiments to obtain more detailed insight into the influence of the considered passage's wake. For comparison, a steady blowing approach was used. The c_μ -values could be estimated much more accurately compared to a previous study due to the data of the conducted actuator slot experiments with an MPT. With the RMPC actuation, a similar static pressure rise of the considered passage was achieved, while the actuation mass flow effort was up to 66% lower depending on the actuation amplitude. This is particularly advantageous because it could be confirmed for the annular test rig

that the efficiency of a passage decreases with increasing actuation amplitude. In summary, AFC can improve an operating condition, but should only be used selectively due to actuation costs. For this purpose, in a periodic operation, an optimal closed-loop controller exploiting the periodicity, such as an RMPC, can be a promising option.

Acknowledgements. The authors gratefully acknowledge the support of the Deutsche Forschungsgemeinschaft (DFG) as part of collaborative research center SFB 1029 “Substantial efficiency increase in gas turbines through direct use of coupled unsteady combustion and flow dynamics” on projects B01 and B06.

References

1. Zander, V., Nitsche, W.: Control of secondary flow structures on a highly loaded compressor cascade. *Proc. IMechE Part A J. Power Energy* **227**(6), 674 (2013)
2. Cattafesta III, L.N., Sheplak, M.: Actuators for active flow control. *Ann. Rev. Fluid Mech.* **43**(1), 247 (2011)
3. Anthoine, J., et al.: *Measurements Techniques in Fluid Dynamics - An Introduction*, 3rd revised edn, Von Karman Institute for Fluid Dynamics, Rhode-Saint-Genese (2009)
4. Fietzke, B., King, R., Mihalyovics J., Peitsch, D.: Binary repetitive model predictive active flow control applied to an annular compressor stator cascade with periodic disturbances. In: *Proceedings of ASME Turbo Expo 2021: Turbomachinery Technical Conference and Exposition*, GT2021-58744, vol. 4, p. V004T05A003 (2021)
5. Schmid, C., Biegler, L.T.: Quadratic programming methods for reduced Hessian SQP. *Comput. Chem. Eng.* **18**(9), 817 (1994)
6. Morrison, D.R., Jacobson, S.H., Sauppe, J.J., Sewell, E.C.: Branch-and-bound algorithms: a survey of recent advances in searching, branching, and pruning. *Discrete Optim.* **19**, 79 (2016)
7. Schäpel, J.S., King, R., Yücel, F., Völzke, F., Paschereit, C.O., Klein, R.: Fuel injection control for a valve array in a shockless explosion combustor. In: *Proceedings of the ASME Turbo Expo 2018: Turbomachinery Technical Conference and Exposition*, GT2018-75295, vol. 6, p. V006T05A007 (2018)
8. Bar-Shalom, Y., Li, X.-R., Kirubarajan, T.: *Estimation with Applications to Tracking and Navigation: Theory Algorithms and Software*. John Wiley & Sons, Hoboken (2004)
9. Cumpsty, N.A., Horlock, J.H.: Averaging nonuniform flow for a purpose. *J. Turbomach.* **128**(1), 120 (2006)
10. Steinberg, S.J., King, R.: Closed-loop active flow control of repetitive disturbances in a linear stator cascade. In: *2018 Flow Control Conference AIAA 2018-3689*, p. 3689 (2018)
11. Steinberg, S.J., King, R.: Efficiency of active flow control in an unsteady stator vane flow field. In: Radespiel, R., Semaan, R. (eds.) *Fundamentals of High Lift for Future Civil Aircraft*. NNFMMMD, vol. 145, pp. 631–648. Springer, Cham (2021). https://doi.org/10.1007/978-3-030-52429-6_38